nature materials

ARTICLES

https://doi.org/10.1038/s41563-020-0720-x

Check for updates

High-performance solar flow battery powered by a perovskite/silicon tandem solar cell

Wenjie Li[1], Jianghui Zheng[2], Bo Hu[3], Hui-Chun Fu[1], Maowei Hu[3], Atilla Veyssal[1], Yuzhou Zhao[1], Jr-Hau He[4,5], T. Leo Liu[3], Anita Ho-Baillie[2,6,7]✉ and Song Jin[1]✉

The fast penetration of electrification in rural areas calls for the development of competitive decentralized approaches. A promising solution is represented by low-cost and compact integrated solar flow batteries; however, obtaining high energy conversion performance and long device lifetime simultaneously in these systems has been challenging. Here, we use high-efficiency perovskite/silicon tandem solar cells and redox flow batteries based on robust BTMAP-Vi/N^{Me}-TEMPO redox couples to realize a high-performance and stable solar flow battery device. Numerical analysis methods enable the rational design of both components, achieving an optimal voltage match. These efforts led to a solar-to-output electricity efficiency of 20.1% for solar flow batteries, as well as improved device lifetime, solar power conversion utilization ratio and capacity utilization rate. The conceptual design strategy presented here also suggests general future optimization approaches for integrated solar energy conversion and storage systems.

The increasing demand for bringing electricity to rural areas poses many challenges but also presents a great opportunity for developing decentralized electrification systems[1,2]. Compared with conventional electrical grids based on large centralized power generation stations that are commonly seen in developed countries, the decentralized electrification approach features lower capital cost, smaller footprint and shorter deployment time, expediting electrification in rural or remote locations. Due to the abundance of solar resources, solar home systems that can deliver energy on demand are considered one of the most feasible decentralized approaches in developing countries[3,4]. Solar home systems usually convert solar energy into electricity using photovoltaic panels and then store electricity in separate energy storage units, such as lead–acid batteries or Li-ion batteries[5]. Devices that integrate solar energy conversion and storage[6,7] in one unit would be an attractive approach for solar home systems. Toward this end, the emerging solar flow batteries (SFBs) that monolithically integrate photoelectrochemical solar cells and redox flow batteries (RFBs) in a single device are very promising. The unique integrated design of SFBs fulfils all the requisite functions for stand-alone solar home systems without using the relatively expensive maximum power point tracking and d.c.–d.c. conversion electronics[5,6], thereby potentially reducing the cost of solar home systems while achieving high efficiency, convenient integrated thermal management and compact device size (Supplementary Note 1, Supplementary Fig. 1 and Supplementary Table 1)[8–12].

Despite the short history of SFBs, considerable progress has been made recently in both mechanistic understandings[10–12] and device demonstrations of SFBs[13–19] (Supplementary Table 2). Among the various crucial metrics to make SFBs competitive for solar home system applications, solar-to-output electricity efficiency (SOEE) and device lifetime have received most attention so far. The highest SOEE of 14.1% so far for SFBs was achieved by integrating III–V tandem solar cells and methyl viologen (MV)/4-hydroxy-2,2,6,6-tetramethylpiperidin-1-oxyl (4-OH-TEMPO) redox couples[11]. Nevertheless, the photocorrosion-prone III–V materials[20,21] and the fast decomposition of the 4-OH-TEMPO redox couple[22,23] greatly limit the lifetime of such SFB devices. Taking advantage of the recent progress in photoelectrode protection[24,25] and stable organic redox couples[26], a recent study using well protected silicon photoelectrodes and robust bis-(trimethylammonio) propyl-functionalized redox couples demonstrated an SFB with a substantially improved continuous operation lifetime of more than 200 h but a lower SOEE of 5.4% (ref. [12]) (Supplementary Fig. 2 shows an itemized comparison between the two aforementioned SFBs). With these advances, the urgency lies in the design and demonstration of a monolithically integrated SFB that can deliver both high SOEE and long lifetime. Bearing these goals in mind, we turn our attention to silicon-based tandem solar cells that possess both high power conversion efficiency (PCE) (due to the wider solar spectrum absorption range[27]) and stable silicon bottom cells, which, with proper protection layers, can prevent corrosion from aqueous electrolytes[28,29]. To achieve the optimal voltage matching between the solar cell and the redox couples, which has been previously shown to be critical for high SOEE in SFBs[11], the tandem junction solar cells need to be carefully designed to ensure not only high PCE but also a suitable photovoltage. The emerging high-efficiency perovskite/silicon tandem cells[30–32] thus stand out because of the exceptional bandgap tunability of the perovskite top layer[33] in a cost-effective manner compared with conventional inorganic top layer materials such as III–V and II–VI (ref. [34]).

Here, we present a $(FAPbI_3)_{0.83}(MAPbBr_3)_{0.17}$ (MA, methylammonium; FA, formamidinium) perovskite/silicon tandem solar cell with high efficiency and suitable photovoltage for aqueous organic

[1]Department of Chemistry, University of Wisconsin—Madison, Madison, WI, USA. [2]Australian Centre for Advanced Photovoltaics, School of Photovoltaic and Renewable Energy Engineering, University of New South Wales (UNSW), Sydney, New South Wales, Australia. [3]Department of Chemistry and Biochemistry, Utah State University, Logan, UT, USA. [4]Division of Computer, Electrical and Mathematical Sciences and Engineering, King Abdullah University of Science and Technology, Thuwal, Saudi Arabia. [5]Department of Materials Science and Engineering, City University of Hong Kong, Kowloon, Hong Kong. [6]The University of Sydney Nano Institute, The University of Sydney, Sydney, New South Wales, Australia. [7]School of Physics, The University of Sydney, Sydney, New South Wales, Australia. ✉e-mail: anita.ho-baillie@sydney.edu.au; jin@chem.wisc.edu

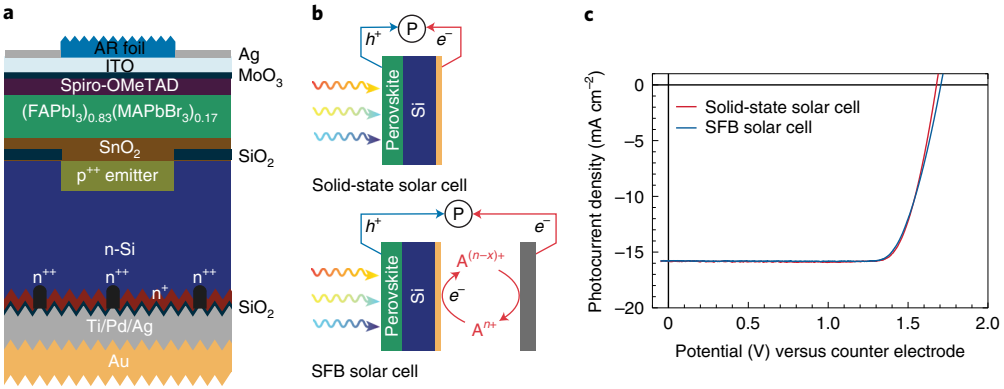

Fig. 1 | Schematic design and solar performance of perovskite/silicon tandem solar cell. a, Architecture of the perovskite/silicon tandem solar cell that consists of an $(FAPbI_3)_{0.83}(MAPbBr_3)_{0.17}$ top cell, a silicon bottom cell and a 100-nm gold bottom protection layer. ITO, indium tin oxide; AR, anti-reflection. **b**, Configuration of the solid-state solar cell and SFB solar cell. In the SFB solar cell configuration, only the gold bottom protection layer is exposed to the electrolyte. **c**, *J*–*V* performance of solid-state perovskite/silicon solar cell and SFB photoelectrode fabricated from the same cell. 0.1-M BTMAP-Vi in 1-M NaCl (prereduced to 50% $BTMAP\text{-}Vi^{4+}$/50% $BTMAP\text{-}Vi^{3+}$) was used as the electrolyte for the SFB photoelectrode measurement.

SFBs. We introduce a theoretical modelling method, which, together with electrochemical study of state-of-the-art aqueous organic RFB redox couples[35–39], predicts that the bis-(trimethylammonio)propyl viologen (BTMAP-Vi) and 4-trimethylammonium-TEMPO (N^{Me}-TEMPO) redox couples can be well matched with the perovskite/silicon tandem solar cells. A simple and effective protection method can make the silicon bottom cell that is exposed to aqueous electrolyte corrosion resistant. Enabled by such rational design, we demonstrate a high SFB SOEE of 20.1%, which effectively utilizes over 90% of the PCE of the perovskite/silicon cell, and an unprecedented continuous operation lifetime of more than 500 h.

Design of perovskite/silicon tandem solar cells

There are three major considerations for designing perovskite/silicon tandem solar cells for high-performance SFBs: suitable photovoltage, high PCE, and good corrosion resistance when in contact with aqueous electrolytes. Previous mechanistic study reveals that, to realize the highest possible SOEE for SFBs with certain solar cells, the maximum power point voltage (V_{MPP}) of the solar cell needs to be matched with the formal cell potential (E_{cell}^0), that is, the cell potential of the SFB or RFB at 50% state of charge (SOC) determined by the formal potentials of the redox couples chosen[11]. Additionally, a higher E_{cell}^0 is generally desired for SFBs since it is beneficial for improving the internal energy conversion efficiency, discharging power density and energy density[40]. Considering the stable operation voltage window of aqueous electrolytes and the stability limitation of redox couples, E_{cell}^0 for aqueous RFBs, especially aqueous organic RFBs, rarely exceeds 1.4 V (refs. [39,41]). On the basis of these considerations, we designed and fabricated $(FAPbI_3)_{0.83}(MAPbBr_3)_{0.17}$ perovskite/silicon tandem solar cells following a previous report[31] (Fig. 1a and Supplementary Fig. 3). Current density–voltage (*J*–*V*) measurements of this solid-state perovskite/silicon solar cell in the configuration shown in Fig. 1b reveal an open-circuit voltage (V_{oc}) of 1.68 V, a short-circuit current density (J_{sc}) of 15.8 mA cm^{-2}, a fill factor of 80.2% and a PCE of 21.3% (Fig. 1c). Importantly, the composition of the $(FAPbI_3)_{0.83}(MAPbBr_3)_{0.17}$ perovskite results in a bandgap well suited for the tandem design, producing a V_{MPP} of 1.38 V, which is in the optimum range for aqueous organic SFBs as discussed above.

To protect the silicon bottom cell from corrosion by aqueous electrolyte, an established method is to deposit $Ti/TiO_2/Pt$ layers on Si[12,15]. However, because no catalyst is needed for SFBs due to the fast kinetics of RFB redox couples, a wide range of stable and conductive materials (such as gold and titanium) can be used to fabricate the protection layers[24,25]. For ease of fabrication, here we deposited a thin (100-nm) layer of gold on the silicon bottom cell using thermal evaporation (Fig. 1a), which proved to be a very robust protection material for silicon in neutral aqueous electrolytes. We then fabricated the photoelectrode using the resultant cell and characterized its solar performance in the solar cell configuration of SFB, in which photogenerated electrons are collected by the $BTMAP^{4+/3+}$ redox couple at the Au–electrolyte interface and regenerated on the carbon felt counter electrode (Fig. 1b). As shown in Fig. 1c, the performance of the photoelectrode (V_{oc}, 1.71 V; J_{sc}, 15.8 mA cm^{-2}; fill factor, 78.3%; PCE, 21.1%) closely resembled that of the solid-state cell, indicating a fast charge transfer at the solid–liquid interface.

SFB performance estimation with theoretical modelling

To quantitatively understand the principles of voltage matching between the E_{cell}^0 of the SFB and V_{MPP} of the solar cell, and determine the exact E_{cell}^0 that can enable the highest SOEE with the perovskite/silicon tandem solar cells, we performed a numerical calculation of SOEE with different hypothetical E_{cell}^0 values. Note that the actual cell potential (E_{cell}) of an SFB changes with SOC and needs to be calculated using the following equation derived from the Nernst equation:

$$E_{cell} = E_{cell}^0 - \frac{RT}{nF}\ln\left[\frac{1-SOC}{SOC}\right]^2 + IR_{DC} \quad (1)$$

where *R* is the universal gas constant, *T* is temperature, *n* is the number of electrons transferred in the redox reaction, *F* is the Faraday constant, *I* is the applied current and R_{DC} is the overall d.c. resistance of the SFB in RFB mode[40] (see Methods, Supplementary Note 2 and Supplementary Fig. 5 for calculation details). Figure 2a presents a series of representative I–E_{cell} lines (calculated with an E_{cell}^0 of 1.34 V) at different SOCs overlaid with the *I*–*V* curve of the perovskite/silicon photoelectrode in solar cell mode (the blue curve in Fig. 1c), from which we can find the operating points marked by the green circles. Building on the concept of instantaneous solar-to-output electricity efficiency ($SOEE_{ins}$)[12], defined as the PCE of the SFB at a specific SOC, we calculated the $SOEE_{ins}$ at different SOCs (Fig. 2b) using the following equation:

$$SOEE_{ins} = \frac{P_{electrical,in}}{P_{illumination}}\,PE_{internal} = \frac{I_{operating}V_{operating}}{SA}\,CE \times VE \quad (2)$$

where $P_{electrical,in}$ is the input electrical power provided by the photoelectrode, $P_{illumination}$ is the illumination power, which can be calculated with the input light irradiance (*S*) and the active area of the

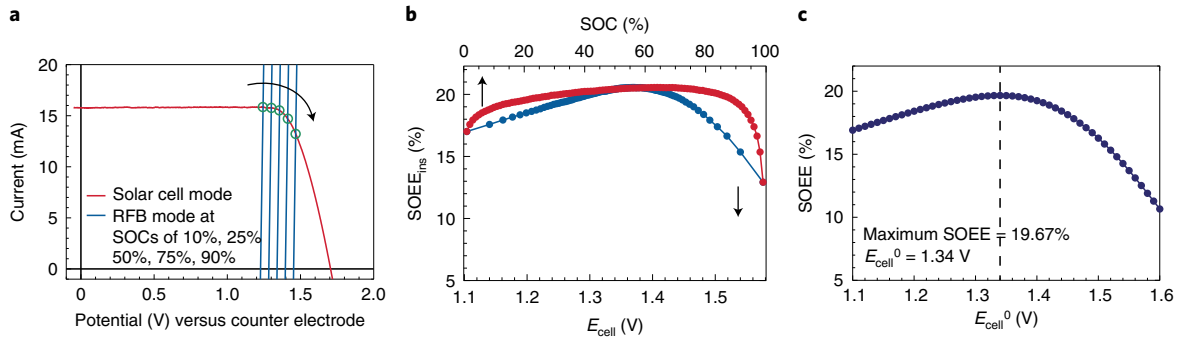

Fig. 2 | Calculation of SOEE as a function of E_{cell}^0. a, Representative overlaid *I*–*V* curves for photoelectrode measured in solar cell mode and RFB mode calculated at different SOCs with an E_{cell}^0 of 1.34 V. Note that the blue lines have a slight inclination (the slope is equal to R_{DC}). The green circles show the operating points at different SOCs, which move alone the photoelectrode *I*–*V* curve as SOC increases. **b**, Representative SOEE$_{ins}$ with respect to SOC and E_{cell}, calculated with an E_{cell}^0 of 1.34 V (more examples calculated with different E_{cell}^0 values are shown in Supplementary Fig. 6). **c**, Calculated SOEE as a function of E_{cell}^0 between 1.10 and 1.60 V, showing a maximum of 19.67% when E_{cell}^0 is 1.34 V.

photoelectrode (A), PE$_{internal}$ is the internal PCE of the SFB, which consists of both Coulombic efficiency (CE) and voltage efficiency (VE), and $I_{operating}$ and $V_{operating}$ are the current and voltage at a specific operating point of the SFB, respectively.

The overall SOEE of an SFB operated between 1% SOC and 99% SOC (98% capacity utilization rate) can be calculated as the integral average of SOEE$_{ins}$ with respect to SOC (Fig. 2b). By repeating the calculation described above with different E_{cell}^0 values from 1.10 to 1.60 V with a 10-mV interval, we reveal the qualitative relationship between SOEE and E_{cell}^0 (Fig. 2c). A maximum SOEE of 19.67% is found at an E_{cell}^0 of 1.34 V. Note that SOEE–E_{cell}^0 and SOEE$_{ins}$–E_{cell} curves convey completely different information and should be carefully differentiated (see Supplementary Fig. 7 for a detailed discussion). This simulation also shows that the best-matched E_{cell}^0 should always be slightly smaller than the V_{MPP} of the solar cell, and the difference between these two points depends on the shape of the solar cell *I*–*V* curve (Supplementary Fig. 8). In addition, this simulation method allows us to estimate the SFB performance under different irradiation conditions and thus predict the behaviour of the SFB under realistic outdoor operating conditions with irradiation fluctuations (Supplementary Note 3 and Supplementary Fig. 9).

Design and electrochemical study of electrolytes

To design the electrolytes for high-performance SFBs, we mainly focused on three aspects: low corrosiveness, good voltage matching and long lifetime. We specifically targeted those redox couples that are soluble and stable at neutral pH to minimize the corrosiveness to solar cells. The SOEE–E_{cell}^0 relationship (Fig. 2c) reveals that E_{cell}^0 needs to be at least 1.25 V to enable an SOEE higher than 19%, which led us to the three redox couple pairs shown in Fig. 3a: $MV^{2+/+}$ and [4-OH-TEMPO]$^{+/\cdot}$ (E_{cell}^0 = 1.26 V)[22], [BTMAP-Vi]$^{4+/3+}$ and [N^{Me}-TEMPO]$^{+/\cdot}$ (E_{cell}^0 = 1.29 V)[36] and [BTMAP-Vi]$^{3+/2+}$ and [FcN]$^{2+/+}$ (FcN, (ferrocenylmethyl)trimethylammonium) (E_{cell}^0 = 1.31 V)[36,42].

The stability of these redox couples was assessed by RFB galvanostatic cycling tests[43] conducted in a nitrogen purge box using electrolytes consisting of 0.10-M redox couples, 1.0-M NaCl as supporting salt and a Selemion AMV anion-exchange membrane (Fig. 3b). The RFBs built with $MV^{2+/+}$ and [4-OH-TEMPO]$^{+/\cdot}$ and with [BTMAP-Vi]$^{3+/2+}$ and [FcN]$^{2+/+}$ showed high capacity fade rates of 9.13% per day and 4.78% per day, respectively, which can be mainly attributed to the fast chemical degradation of [4-OH-TEMPO]$^{+/\cdot}$ and [BTMAP-Vi]$^{3+/2+}$ redox couples[22,36]. In contrast, the RFB built with [BTMAP-Vi]$^{4+/3+}$ and [N^{Me}-TEMPO]$^{+/\cdot}$ exhibited a particularly low temporal capacity fade rate of 0.60% per day, which is among the most stable aqueous organic RFBs reported so far[35,36]. Despite the fact that BTMAP-Vi is considered one of the most stable redox couples for aqueous organic RFBs[26], we found that it is only stable when the reduction reaction is limited to the first redox state at −0.353 V (Supplementary Fig. 10). Detailed characterizations of the [BTMAP-Vi]$^{4+/3+}$/[N^{Me}-TEMPO]$^{+/\cdot}$ redox couples were further carried out using cyclic voltammetry (CV), RFB galvanostatic cycling, d.c. polarization, ^{1}H-NMR and rotating disc electrode (RDE) measurements (Supplementary Figs. 11–16), which confirmed the fast kinetics and very low membrane crossover of these redox species. In particular, open-circuit voltage measurement revealed an actual E_{cell}^0 of 1.26 V for the [BTMAP-Vi]$^{4+/3+}$/[N^{Me}-TEMPO]$^{+/\cdot}$ RFB (Supplementary Fig. 13a), which is very close to the E_{cell}^0 of 1.29 V estimated from CV shown in Fig. 3a.

Characterization and analysis of integrated SFB device

After carefully validating the individual components, we built the SFB device using well characterized perovskite/silicon photoelectrode and BTMAP-Vi/N^{Me}-TEMPO redox couples (Supplementary Fig. 17). The SFB can be switched among three operating modes: solar cell mode, solar recharge mode and RFB mode (Supplementary Fig. 18). The cycling test of the SFB was performed by first charging the device in solar recharge mode with simulated solar irradiation until E_{cell} reached the upper cutoff potential of 1.5 V (instead of a time cutoff) to ensure a near-unit capacity utilization rate. The device was then discharged galvanostatically in RFB mode until E_{cell} reached the lower cutoff potential of 0.8 V. To match the average photocurrent during the solar charging process, a discharging current of 15 mA (3.75 mA cm^{-2}, on the basis of the area of the carbon felt electrode) was applied. The photocurrent and cell potential (blue and red curves in Fig. 4a, respectively) were monitored during the cycling test with two synchronized potentiostat channels.

The SFB was continuously cycled for 426 cycles (516 h) and maintained a very stable performance during the whole time of operation. The actual SOEE of the SFB device is calculated using the photocurrent/cell voltage data as shown in Fig. 4a (see Methods for calculation details). We observed a slight increase of SOEE in the first 51 cycles from 18.9% to 20.1%, and it then stabilized around 20.1% during the rest of the cycling period (Fig. 4c). To further analyse the cycling behaviour of the SFB, we calculated the experimental SOEE$_{ins}$ with respect to SOC using equation (2). Figure 4b shows that the overall SOEE$_{ins}$ increases from cycle 1 to cycle 51, owing to the increase of photocurrent density (Supplementary Fig. 19), and remains unchanged from cycle 51 to cycle 401. Moreover, the shape of the SOEE$_{ins}$–SOC curve also changes from a near-symmetrical rise–decay shape to a continuous rise shape. In light of the simulated SOEE$_{ins}$–SOC curve shape discussed previously (Supplementary

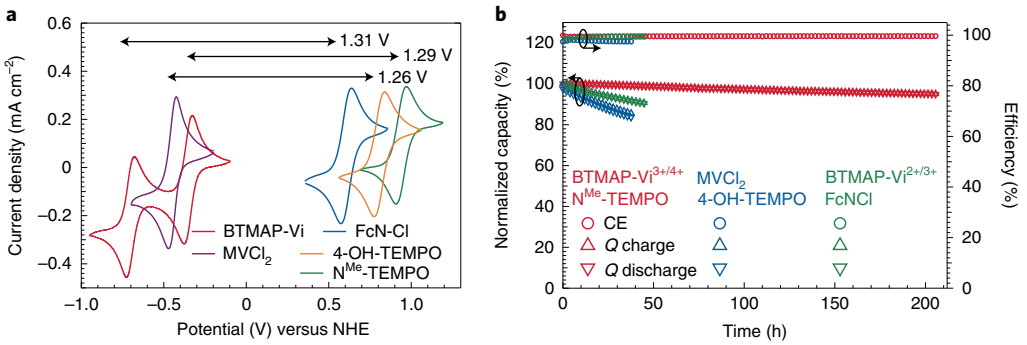

Fig. 3 | Electrochemical characterization of redox couples and RFBs. a, Cyclic voltammograms of three different aqueous organic RFB redox couple pairs that can enable an E_{cell}^0 higher than 1.25 V. All voltammograms are scanned at 10 mV s^{-1} on a glassy carbon electrode using electrolytes containing 5.0-mM active redox species and 1.0-M NaCl. NHE, normal hydrogen electrode. **b**, RFB normalized capacity and CE during galvanostatic cycling at 2.5 mA cm^{-2} with different redox couple pairs, showing the outstanding stability of the BTMAP-Vi/N^{Me}-TEMPO RFB.

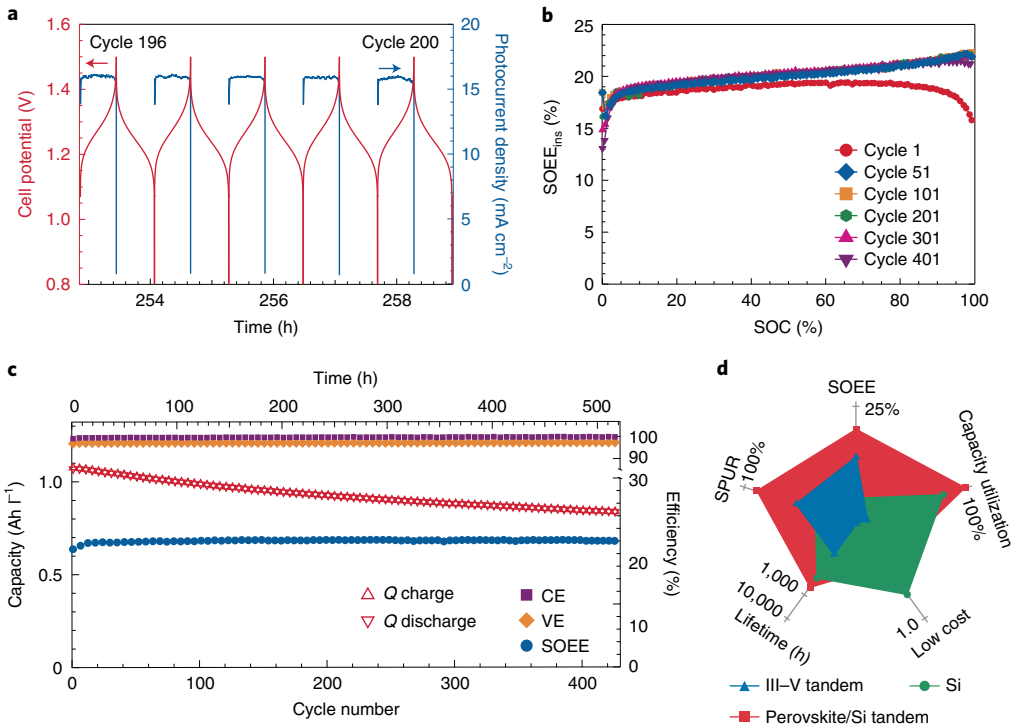

Fig. 4 | Performance of integrated SFB built with perovskite/silicon solar cell and BTMAP-Vi/N^{Me}-TEMPO redox couples. a, Representative device cycling behaviour of the SFB between cycle 196 and cycle 200. The cell potential was measured in RFB mode and the photocurrent density was measured in SFB solar recharge mode. **b**, $SOEE_{ins}$–SOC calculated using the experimental photocurrent/cell potential data shown in **a**. Other than a slight improvement of $SOEE_{ins}$ from cycle 1 to cycle 51, the SFB maintained a very stable $SOEE_{ins}$–SOC profile during the cycling period. **c**, Charge and discharge capacity, CE, VE and SOEE of SFB over 426 cycles. The data are downsampled to show one data point in every five cycles for better visibility. **d**, Comparison of the SFB performance metrics reported in this work with the other two previously demonstrated SFBs in a multivariate radar chart. The axis limits are set to 25%, 100%, 10,000 h (in log scale) and 100% for SOEE, SPUR, lifetime and capacity utilization rate, respectively. The relative cost of each SFB was estimated on the basis of a 'low-cost factor' (Supplementary Fig. 2).

Fig. 6), we hypothesized that this curve shape change is caused by an increase of the best-matched E_{cell}^0 for the perovskite/silicon photoelectrode (E_{cell} of the SFB was controlled by cutoff voltages and thus less likely to change). Indeed, after the cycling test, characterization of the photoelectrode in solar cell mode again revealed increases in both photocurrent and photovoltage, resulting in an overall PCE improvement from 21.1% to 22.3% (Supplementary Fig. 20a). The SOEE–E_{cell}^0 relationship calculated using the J–V data of the photoelectrode after cycling showed that the best-matched E_{cell}^0 increased from 1.34 V to 1.36 V, which validates our model that uses the shape of the $SOEE_{ins}$–SOC curve to qualitatively diagnose changes of the best-matched E_{cell}^0 during operation. As expected from the RFB cycling tests (Fig. 3b), the total capacity of the SFB decreased from 1.075 Ah l^{-1} to 0.883 Ah l^{-1} (calculated on the basis of the total volume of anolyte and catholyte) during the cycling test (Supplementary Fig. 21), which indicates that the major limiting factor for the lifetime of this SFB is the stability of redox couples (more specifically, probably N^{Me}-TEMPO). Over the whole cycling

period, the SFB delivered an average discharge energy of 1.16 Wh l^{-1} with a near-unit CE and VE of 99.8% and 97.3%, respectively (Fig. 4c). We further tested another SFB device using higher concentrations of the redox couples (0.5 M and 1.0 M) in longer (>7-h) charge/discharge cycles to show that the high SFB performance is maintained at a more practical higher discharge energy density of 13.14 Wh l^{-1} (Supplementary Fig. 22).

Importantly, the average SOEE of 20.1% achieved by the SFB shown in Fig. 4 is more than 40% higher than the previous record efficiency of 14.1% for integrated solar rechargeable battery devices[11]. Furthermore, due to the good voltage match between the perovskite/silicon tandem solar cell and the BTMAP-Vi/N^{Me}-TEMPO redox couples, we are able to achieve the substantially increased SOEE with a solar cell that exhibits a PCE of only 22.3% (the highest value after cycling test), which is much lower than the PCE of the III–V tandem solar cell (26.1%) used in the previous record-holding SFB[11]. Naturally, the ratio between SOEE and PCE can be used as a quantitative measure of the voltage match between photoelectrodes and redox couples, and we propose to name it the 'solar power conversion utilization ratio (SPUR)'. SPUR is a new and important figure of merit for SFBs, as it characterizes how effectively the solar energy conversion ability of the photoelectrodes can be extracted in the SFBs. It is also worth noting that, because of the SOC dependence of $SOEE_{ins}$, it is not possible to achieve 100% SPUR even with the best-matched E_{cell}^0. The SFB device demonstrated here exhibits a SPUR of 90.1%, which is very close to the theoretical maximum of 95.5% achievable with the perovskite/silicon solar cell and almost twice the next highest value reported for the SFB device based on the III–V tandem cell[11]. A detailed analysis and comparison of the voltage match and SPUR between the two SFB devices (Supplementary Fig. 23) reveals the reasons for such substantial improvements. In addition to the SOEE and SPUR, capacity utilization rate, lifetime and cost are also important for SFBs. By qualitatively plotting the five most important metrics for SFBs in a radar plot, we can clearly see that, unlike the other two previously reported SFBs, which can cover only a few performance dimensions well, the SFB powered by the perovskite/silicon solar cell can deliver good performance in all the dimensions (Fig. 4d).

Conclusions

This work presents a monolithically integrated SFB device based on perovskite/silicon tandem solar cells that features important breakthroughs in several dimensions, including SOEE, SPUR, capacity utilization rate and device lifetime, without compromising low fabrication cost. The $(FAPbI_3)_{0.83}(MAPbBr_3)_{0.17}$ perovskite/silicon tandem solar cell rationally designed specifically for aqueous organic SFBs not only delivers high efficiency, but the cost-effective perovskite-compatible method of fabricating the electrolyte contact for silicon bottom cell also enables good stability and device lifetime. We have also developed a numerical calculation method that has not only guided us to the selection of BTMAP-Vi/N^{Me}-TEMPO redox couples to match the perovskite/silicon cells and achieve a high SOEE and SPUR, but also shed light on the deeper conceptual understanding of the voltage matching principles for integrated solar storage technologies in general. These results constitute a major advance toward a practical approach of using integrated SFBs for solar home systems and other distributed solar power generation and storage applications.

Online content

Any methods, additional references, Nature Research reporting summaries, source data, extended data, supplementary information, acknowledgements, peer review information; details of author contributions and competing interests; and statements of data and code availability are available at https://doi.org/10.1038/s41563-020-0720-x.

Received: 9 January 2020; Accepted: 29 May 2020;
Published online: 13 July 2020

References

1. Eke, K. P. Emerging considerations of rural electrification infrastructure development in Africa. In *2017 IEEE PES Power Africa Conference* 138–142 (IEEE, 2017).
2. Cook, P. Infrastructure, rural electrification and development. *Energy Sustain. Dev.* **15**, 304–313 (2011).
3. Wamukonya, N. Solar home system electrification as a viable technology option for Africa's development. *Energy Policy* **35**, 6–14 (2007).
4. Halder, P. K. Potential and economic feasibility of solar home systems implementation in Bangladesh. *Renew. Sustain. Energy Rev.* **65**, 568–576 (2016).
5. Charles, R. G., Davies, M. L., Douglas, P., Hallin, I. L. & Mabbett, I. Sustainable energy storage for solar home systems in rural Sub-Saharan Africa—a comparative examination of lifecycle aspects of battery technologies for circular economy, with emphasis on the South African context. *Energy* **166**, 1207–1215 (2019).
6. Gurung, A. & Qiao, Q. Q. Solar charging batteries: advances, challenges, and opportunities. *Joule* **2**, 1217–1230 (2018).
7. Schmidt, D., Hager, M. D. & Schubert, U. S. Photo-rechargeable electric energy storage systems. *Adv. Energy Mater.* **6**, 1500369 (2015).
8. Yu, M. et al. Solar-powered electrochemical energy storage: an alternative to solar fuels. *J. Mater. Chem. A* **4**, 2766–2782 (2016).
9. Wedege, K., Bae, D., Smith, W. A., Mendes, A. & Bentien, A. Solar redox flow batteries with organic redox couples in aqueous electrolytes: a minireview. *J. Phys. Chem. C* **122**, 25729–25740 (2018).
10. Wedege, K. et al. Unbiased, complete solar charging of a neutral flow battery by a single Si photocathode. *RSC Adv.* **8**, 6331–6340 (2018).
11. Li, W., Fu, H.-C., Zhao, Y., He, J.-H. & Jin, S. 14.1% efficient monolithically integrated solar flow battery. *Chem* **4**, 2644–2657 (2018).
12. Li, W. J. et al. A long lifetime aqueous organic solar flow battery. *Adv. Energy Mater.* **9**, 1900918 (2019).
13. Yu, M. Z. et al. Aqueous lithium-iodine solar flow battery for the simultaneous conversion and storage of solar energy. *J. Am. Chem. Soc.* **137**, 8332–8335 (2015).
14. Liao, S. et al. Integrating a dual-silicon photoelectrochemical cell into a redox flow battery for unassisted photocharging. *Nat. Commun.* **7**, 11474–11478 (2016).
15. Li, W. et al. Integrated photoelectrochemical solar energy conversion and organic redox flow battery devices. *Angew. Chem. Int. Ed.* **55**, 13104–13108 (2016).
16. Wedege, K., Azevedo, J., Khataee, A., Bentien, A. & Mendes, A. Direct solar charging of an organic-inorganic, stable, and aqueous alkaline redox flow battery with a hematite photoanode. *Angew. Chem. Int. Ed.* **55**, 7142–7147 (2016).
17. Cheng, Q. et al. Photorechargeable high voltage redox battery enabled by Ta_3N_5 and GaN/Si dual-photoelectrode. *Adv. Mater.* **351**, 1700312–1700318 (2017).
18. McKone, J. R., DiSalvo, F. J. & Abruna, H. D. Solar energy conversion, storage, and release using an integrated solar-driven redox flow battery. *J. Mater. Chem. A* **5**, 5362–5372 (2017).
19. Zhou, Y. et al. Efficient solar energy harvesting and storage through a robust photocatalyst driving reversible redox reactions. *Adv. Mater.* **103**, 1802294–1802297 (2018).
20. Hu, S. et al. Amorphous TiO_2 coatings stabilize Si, GaAs, and GaP photoanodes for efficient water oxidation. *Science* **344**, 1005–1009 (2014).
21. Khan, M. A. et al. Importance of oxygen measurements during photoelectrochemical water-splitting reactions. *ACS Energy Lett.* **4**, 2712–2718 (2019).
22. Liu, T., Wei, X., Nie, Z., Sprenkle, V. & Wang, W. A total organic aqueous redox flow battery employing a low cost and sustainable methyl viologen anolyte and 4-HO-TEMPO catholyte. *Adv. Energy Mater.* **6**, 1501449 (2015).
23. Liu, Y. et al. A long lifetime all-organic aqueous flow battery utilizing TMAP-TEMPO radical. *Chem* **5**, 1861–1870 (2019).
24. Hu, S. et al. Thin-film materials for the protection of semiconducting photoelectrodes in solar-fuel generators. *J. Phys. Chem. C* **119**, 24201–24228 (2015).
25. Bae, D., Seger, B., Vesborg, P. C. K., Hansen, O. & Chorkendorff, I. Strategies for stable water splitting via protected photoelectrodes. *Chem. Soc. Rev.* **46**, 1933–1954 (2017).
26. Beh, E. S. et al. A neutral pH aqueous organic-organometallic redox flow battery with extremely high capacity retention. *ACS Energy Lett.* **2**, 639–644 (2017).
27. Green, M. A. et al. Solar cell efficiency tables (version 54). *Prog. Photovolt.* **27**, 565–575 (2019).
28. Seger, B. et al. Using TiO_2 as a conductive protective layer for photocathodic H_2 evolution. *J. Am. Chem. Soc.* **135**, 1057–1064 (2013).

29. Shaner, M. R., Hu, S., Sun, K. & Lewis, N. S. Stabilization of Si microwire arrays for solar-driven H_2O oxidation to O_2(g) in 1.0 M KOH(aq) using conformal coatings of amorphous TiO_2. *Energy Environ. Sci.* **8**, 203–207 (2015).
30. Zheng, J. H. et al. Large area efficient interface layer free monolithic perovskite/homo-junction-silicon tandem solar cell with over 20% efficiency. *Energy Environ. Sci.* **11**, 2432–2443 (2018).
31. Zheng, J. H. et al. 21.8% efficient monolithic perovskite/homo-junction-silicon tandem solar cell on 16 cm(2). *ACS Energy Lett.* **3**, 2299–2300 (2018).
32. Bush, K. A. et al. 23.6%-efficient monolithic perovskite/silicon tandem solar cells with improved stability. *Nat. Energy* **2**, 17009 (2017).
33. Correa-Baena, J. P. et al. Promises and challenges of perovskite solar cells. *Science* **358**, 739–744 (2017).
34. Yu, Z. S., Leilaeioun, M. & Holman, Z. Selecting tandem partners for silicon solar cells. *Nat. Energy* **1**, 16137 (2016).
35. Ji, Y. et al. A phosphonate-functionalized quinone redox flow battery at near-neutral pH with record capacity retention rate. *Adv. Energy Mater.* **9**, 1900039 (2019).
36. DeBruler, C. et al. Designer two-electron storage viologen anolyte materials for neutral aqueous organic redox flow batteries. *Chem* **3**, 961–978 (2017).
37. Park, M., Ryu, J., Wang, W. & Cho, J. Material design and engineering of next-generation flow-battery technologies. *Nat. Rev. Mater* **2**, 16080–16018 (2016).
38. Hollas, A. et al. A biomimetic high-capacity phenazine-based anolyte for aqueous organic redox flow batteries. *Nat. Energy* **3**, 508–514 (2018).
39. Luo, J. A., Hu, B., Hu, M. W., Zhao, Y. & Liu, T. L. Status and prospects of organic redox flow batteries toward sustainable energy storage. *ACS Energy Lett.* **4**, 2220–2240 (2019).
40. Weber, A. Z. et al. Redox flow batteries: a review. *J. Appl. Electrochem.* **41**, 1137–1164 (2011).
41. Darling, R. M., Gallagher, K. G., Kowalski, J. A., Ha, S. & Brushett, F. R. Pathways to low-cost electrochemical energy storage: a comparison of aqueous and nonaqueous flow batteries. *Energy Environ. Sci.* **7**, 3459–3477 (2014).
42. Hu, B., DeBruler, C., Rhodes, Z. & Liu, T. L. Long-cycling aqueous organic redox flow battery (AORFB) toward sustainable and safe energy storage. *J. Am. Chem. Soc.* **139**, 1207–1214 (2017).
43. Goulet, M. A. & Aziz, M. J. Flow battery molecular reactant stability determined by symmetric cell cycling methods. *J. Electrochem. Soc.* **165**, A1466–A1477 (2018).

Methods

Electrochemical measurements. CV measurements were conducted using a Bio-Logic SP-200/BP-300/VMP3 potentiostat. A 3-mm-diameter glassy carbon disc electrode (BASi or CH Instruments) was used as the working electrode, which was polished using 0.3-μm and 0.05-μm alumina slurry to mirror polish and washed with deionized water (Milli-Q, 18.2 MΩ cm) and methanol before each test. The glassy carbon electrode was further cleaned electrochemically in 1-M Na_2SO_4 solution (with 1-mM potassium ferrocyanide as internal reference) by sweeping the potential between −1.0 V and 1.5 V versus the reference electrode at 100 mV s^{-1} until the peak separation of the ferrocyanide/ferricyanide redox couple reaches about 60 mV. A Pt wire electrode (0.5-mm diameter) and a saturated calomel electrode (CH Instruments) were used as the counter- and reference electrodes, respectively. The electrolyte consisted of 5-mM active redox material and 1.0-M NaCl and was purged with inert gas (argon or nitrogen) before measurements. CV was scanned at a rate of 10 mV s^{-1} and the formal potentials of the redox couples were estimated by calculating the average potential between the anodic peak and cathodic peak in the CV curves. Electrochemical kinetics of N^{Me}-TEMPO was studied using an RDE setup (BASi, RDE-2) at different rotating speeds (Supplementary Fig. 16). A 3-mm-diameter glassy carbon RDE (BASi) was cleaned as described before and used as the working electrode. Counter- and reference electrodes were the same as those in CV measurements. Linear scan voltammetry (LSV) was carried out at a scan rate of 10 mV s^{-1} from 0.4 V to 1.0 V versus the saturated calomel electrode. The diffusion coefficient (D_R) of the reduced N^{Me}-TEMPO was calculated using the Levich equation, $i_l = 0.62nFAD^{2/3}\omega^{1/2}\upsilon^{-1/6}C$, where $n = 1$, $F = 96{,}485$ C mol^{-1}, electrode area $A = 0.0707$ cm^2, N^{Me}-TEMPO concentration $C = 5.0 \times 10^{-6}$ mol cm^{-3}, $\upsilon = 0.9380 \times 10^{-2}$ cm^2 s^{-1} (kinematic viscosity of 1.0-M NaCl at 298 K), ω is rotation rate and the limiting current (i_l) was determined at an overpotential (η) of 250 mV. Koutecký–Levich plots ($1/i$ versus $\omega^{-1/2}$) were used to determine the kinetic currents (i_k) at different overpotentials by extrapolating the fitted $1/i$ versus $\omega^{-1/2}$ lines to $\omega^{-1/2} = 0$. To calculate the standard rate constant (k_0) and charge transfer coefficient (α, reduction reaction) of N^{Me}-TEMPO, a Tafel plot (log i_k versus η) was linearly fitted in an η region of 40–80 mV to yield slope and y-intercept values. On the basis of the Butler–Volmer equation for a one-electron oxidation reaction, slope $= (1-\alpha)F/(2.3RT)$, y intercept $= \log(FAk_0C)$.

Fabrication of RFB and integrated SFB device. The RFB and SFB measurements were carried out in a custom-made zero-gap device, similar to what was reported previously[11]. In brief, graphite plates (1/8-inch thickness, MWI) were used as the current collector for RFB devices. Modified current collectors with an additional 15×15 mm^2 clearance window at the centre of the square pocket were used for SFB devices to allow direct contact between the photoelectrode and liquid electrolyte. 20×20 mm^2 graphite felts (GFD 3 EA, SIGRACELL) were pretreated at 400 °C in air for 6 h before being used as electrodes on both sides of the cell. 25×25 mm^2 Selemion AMV (Asahi Glass Co.) was used as an anion-exchange membrane. The membrane was soaked in 1.0-M NaCl solution for more than 24 h before use.

General RFB measurements. N^{Me}-TEMPO and FcNCl were synthesized following the method described in the previous report[36]. Solutions of 0.1-M redox-active molecules in 1.0-M NaCl (5.0 ml) were used as the electrolytes for RFB tests. The RFB was kept in a nitrogen purge box (Terra Universal) during the whole RFB test. The electrolytes were purged with nitrogen for at least 1 h before tests. The electrolyte flow rate was controlled at 20 ml min^{-1} for all RFB measurements.

The RFB cycling and polarization performance tests were carried out using a Bio-Logic BP-300 or SP-200 potentiostat. Galvanostatic cycling tests were performed by charging and discharging the device at a desired constant current density with the following potential windows: 0.7–1.5 V for $MV^{2+/+}$ and $[4\text{-OH-TEMPO}]^{+/\cdot}$, 0.8–1.6 V for $[BTMAP\text{-}Vi]^{4+/3+}$ and $[N^{Me}\text{-TEMPO}]^{+/\cdot}$, 1.1–1.6 V for $[BTMAP\text{-}Vi]^{3+/2+}$ and $[FcN]^{2+/+}$ and 0.5–1.1 V for $[BTMAP\text{-}Vi]^{4+/3+}$ and $[FcN]^{2+/+}$. Figure 3b shows the normalized capacity–time profile for the RFBs during cycling tests, from which the temporal capacity fade rate of each RFB can be calculated using the following equation: capacity fade rate $= \frac{\text{capacity}(t_0) - \text{capacity}(t_1)}{\text{capacity}(t_0)(t_1 - t_0)}$. The capacity fade rate for these full cell RFB tests is a measure of the overall RFB stability that can be affected by many factors, including both the degradation and membrane crossover of the anolyte/catholyte redox couples[43]. To measure the open-circuit voltage of the RFB at different SOCs, the battery was galvanostatically charged or discharged with a 10% SOC step and then rested for 2 min to measure the open-circuit voltage. The 0% SOC and 100% SOC were accessed by the galvanostatic–potentiostatic cycling method until the current density reached 1 mA cm^{-2} at cutoff potentials[12]. The RFB was kept at open circuit for 20 min to reach a stable measurement of open-circuit voltage for 0% and 100% SOC. In the cell polarization characterization, LSV was performed at a scan rate of 100 mV s^{-1}. Forward scan (0 V to 1.6 V) was used at 0% SOC and backward scan (1.6 V to 0 V) was used for all the other SOCs to minimize SOC swing during the LSV test. To further avoid the disturbance of the SOC by LSV scans, the RFB was completely discharged to 0% SOC and then recharged to the specific SOC before each LSV was measured. All the SOCs mentioned in this study were calculated on the basis of the capacity determined by the galvanostatic–potentiostatic cycling method. Potentiostatic electrochemical impedance spectroscopy measurement of the RFB was performed at 0% SOC, with a voltage offset of 10 mV, a bias potential equal to its open-circuit voltage, and frequencies ranging from 100 kHz to 1 Hz.

Fabrication of photoelectrode assembly for integrated SFB device. For fabrication of the $(FAPbI_3)_{0.83}(MAPbBr_3)_{0.17}$ perovskite/homojunction silicon tandem solar cell, an n-type ⟨100⟩ floating zone 1–5-Ω-cm silicon wafer with a thickness of 300 μm was used to prepare the bottom silicon cell with a 130.0-Ω-per-square n^+ high–low junction, 15.1-Ω-per-square p^{++} (from BBr_3) front emitter and n^{++} (from $POCl_3$)-doped rear contacts completed by a Ti/Pd/Ag metal stack. The rest of the non-contacted rear was passivated by thermally grown and annealed SiO_2. The p^{++} area was defined to 1 cm^2 as the active area with thermally grown SiO_2 covering the non-contacted area. To complete full tandem fabrication, the surfaces of front-polished silicon solar cells were treated using ultraviolet ozone cleaner for 6 min before SnO_2 electron transport layer deposition. The SnO_2 colloidal suspension (Alfa Aesar, tin IV oxide, 15% in H_2O colloidal dispersion) was diluted with water to 3.75% and then deposited as the electron transport layer by spin-coating on the front of the silicon solar cells at 3,000 rpm for 30 s and annealing at 100 °C for 20 min. After cooling, the SnO_2-coated silicon substrates were directly transferred to the N_2-filled glovebox for fabrication of the perovskite absorber and hole transport layer. The perovskite precursor solution was prepared by dissolving FAI (1 M), lead iodide (1.1 M), MABr (0.2 M) and lead bromide (0.2 M) in a mixed solvent of *N*,*N*-dimethylformamide and dimethylsulfoxide (4:1 v/v). The perovskite precursor was spin-coated on the SnO_2-coated silicon bottom cell at 2,000 rpm for 20 s, followed by 6,000 rpm for 30 s. During the spin-coating, 100 μl chlorobenzene was quickly dispensed 5 s before the end of the spin process. The film was annealed at 100 °C for 10 min, producing a dark-brown dense perovskite film. The hole transport layer precursor was prepared by dissolving 72.3 mg 2,2′,7,7′-tetrakis(*N*,*N*-di-*p*-methoxyphenylamine)-9,9-spirobifluorene (spiro-OMeTAD), 28.8 μl 4-tert-butylpyridine, 17.4 μl lithium bis(trifluoromethylsulfonyl)imide solution (520 mg ml^{-1} in acetonitrile) and 8 μl FK209-cobalt(III)-TFSI solution (300 mg of FK209-cobalt(III)-TFSI in 1 ml of acetonitrile) in 1 ml chlorobenzene. The spiro-OMeTAD precursor was then deposited onto the perovskite layer by spin-coating at 3,000 rpm for 30 s. An 18-nm MoO_x buffer layer and 100-nm indium tin oxide transparent contact were then deposited sequentially using thermal evaporation and radiofrequency sputtering, respectively. A metal contact grid of silver with a thickness of 230 nm was deposited by thermal evaporation defining the area of 1.0 cm^2, aligning well with the p^{++} silicon emitter area (Supplementary Fig. 4).

The photoelectrode assembly for the integrated SFB device characterization was fabricated using a method similar to that described in a previous report[12]. In brief, the perovskite/silicon tandem cell was affixed onto a custom-made graphite current collector using epoxy resin (Hysol 9460) to cover the window of the current collector. The electrolyte can directly contact the back side of the silicon cell through the window of the current collector and harvest the photogenerated charges during SFB device operation in solar recharge mode and solar cell mode. Ohmic contact to the photoelectrode was made by attaching a copper foil onto the front silver metal contact area of the cell with a Ga/In eutectic mixture (Sigma Aldrich) and fixed with silver paint (Ted Pella, PELCO colloidal silver). The ohmic contact area was then sealed using epoxy resin.

Solid-state and SFB solar cell characterization of perovskite/silicon cell. Solid-state *J*–*V* performance of the perovskite/silicon cells was measured in a two-electrode configuration by making ohmic contact to the front and back sides of the cell with a tungsten probe and copper plate. The *J*–*V* data were collected using a Bio-Logic SP-200 potentiostat under 1 Sun (100 mW cm^{-2}) of AM1.5G simulated illumination by a Newport model 91191 xenon arc lamp solar simulator with a scan rate of 100 mV s^{-1}. The illumination intensity of the AM1.5G solar simulator was calibrated to 100 mW cm^{-2} with a silicon photodiode before *J*–*V* measurements. Note that the design area of the perovskite/silicon tandem in this work is 1.0 cm^2 (the p^{++} diffusion area, SiO_2 insulating open area and silver grid metal surrounding the open area are all 1.0 cm^2); there is no difference in the *J*–*V* measurements with and without using the 1.0-cm^2 metal shadow mask (Supplementary Fig. 4).

The solar performance of the perovskite/silicon photoelectrodes was measured in the assembled SFB device with a Bio-Logic BP-300 potentiostat and 1 Sun (100 mW cm^{-2}) of simulated solar illumination provided using the same xenon arc lamp as mentioned above. The light was guided by a branched flexible silica light guild (Taiopto MEMS International) fed through a N_2 flush box and collimated by an OSL2COL convex lens collimation tube (Thorlabs). The illumination intensity inside the N_2 purge box with light guide and collimator was calibrated to generate the same short-circuit current (I_{sc}) of the solid-state perovskite/silicon tandem junction cell as measured under 1 Sun of AM1.5G simulated solar light outside the box. The photoelectrode measurements were performed in a two-electrode configuration in SFB solar cell mode (Supplementary Fig. 18) with the same electrolytes as used in the RFB test (0.1-M N^{Me}-TEMPO as anolyte and 0.1-M BTMAP-Vi as catholyte in 1.0-M NaCl as supporting electrolyte). The electrolytes were precharged to 50% SOC before solar measurements. A flow rate of 20 ml min^{-1} was used for all the solar measurements. All *J*–*V* curves were recorded at a scan rate of 100 mV s^{-1} without correcting for any uncompensated resistance losses. To confirm the lack of hysteresis in the solid-state solar cell and

SFB photoelectrode J–V behaviours, a reverse scan (from the V_{oc} to J_{sc} direction) was first performed, followed by a forward scan (from the J_{sc} to V_{oc} direction) (Supplementary Fig. 22a). Reverse-scan J–V curves are shown in all other figures and used in the SOEE simulation.

SFB performance estimation with theoretical modelling. To quantitatively evaluate the solar conversion and energy storage efficiency of the integrated SFB device, a specific figure of merit should be considered: SOEE, which is defined by the ratio of the usable electrical energy delivered by the integrated SFB device ($E_{electrical,out}$) at a later time over the total solar energy input ($E_{illumination}$). The SOEE can be calculated using the following equation[15]:

$$\mathrm{SOEE} = \frac{E_{electrical,out}}{E_{illumination}} = \frac{\int I_{out} V_{out}\, dt}{\int SA\, dt}$$

where I_{out} is the output (discharging) current, V_{out} is the output voltage, S is the average incident solar irradiance and A is the total illumination area of the perovskite/silicon photoelectrode (1.0 cm^2). Note that this SOEE is the round-trip efficiency of the delivered electrical energy at any time on demand over the original solar energy input.

The hypothetical overlaid J–V curves of photoelectrodes shown in Fig. 2a illustrate that the operating point for the integrated SFB device could be substantially influenced by the working voltage matching between the photoelectrode and the SFB cell potential. Even though the I–V characteristic of the photoelectrode generally remains unchanged at different SOCs, the SFB cell potential may vary greatly during its charging/discharging process, resulting in a considerable SOEE change at different SOCs. To quantitatively analyse such an SOEE change at different SOCs, $\mathrm{SOEE_{ins}}$ can be defined and estimated using the following equation[12]:

$$\mathrm{SOEE_{ins}} = \frac{P_{electrical,out}}{P_{illumination}} \approx \frac{P_{electrical,in}\ \mathrm{PE_{internal}}}{P_{illumination}} = \frac{I_{operating} V_{operating}}{SA}\ \mathrm{CE}\times\mathrm{VE}$$

where $P_{electrical,out}$ is the electrical discharging power of the SFB; $\mathrm{PE_{internal}}$ can be estimated as the arithmetic product of the CE and VE of the SFB; $I_{operating}$ is the operating photocurrent provided by the photoelectrode during the solar recharging process and $V_{operating}$ is the cell potential measured at the same time as $I_{operating}$.

To find the cell voltage profile of the SFB, we used a simple battery model assuming ideal Nernstian behaviour and constant d.c. resistance[40]. Thus, the cell potential can be calculated using equation (1).

$$E_{cell} = E^0_{cell} - \frac{RT}{nF}\ln\left[\frac{1-\mathrm{SOC}}{\mathrm{SOC}}\right]^2 + IR_{DC} \quad (1)$$

Note that $E_{cell}{}^0$ generally remains constant with a given anolyte/catholyte combination ($E_{cell}{}^0 = E_{anolyte}{}^0 - E_{catholyte}{}^0$, where $E_{anolyte}{}^0$ and $E_{catholyte}{}^0$ are the formal potentials for anolyte and catholyte, respectively). Because the operating current will not be higher than the J_{sc} of the perovskite/silicon solar cell and R_{DC} is around 1.1 Ω (Supplementary Fig. 5c), IR_{DC} (<20 mV) does not contribute substantially to E_{cell} and is neglected in the calculation for simplicity. E_{cell} is calculated from 1% SOC to 99% SOC with an increment of 1% using an arbitrary $E_{cell}{}^0$ to find $V_{operating}$ ($V_{operating} = E_{cell}$ in this case) at different SOCs. Because IR_{DC} is neglected, $I_{operating}$ can be easily found from the I–V curve of the perovskite/silicon photoelectrode in solar cell mode and thus $\mathrm{SOEE_{ins}}$ can be calculated as described above. The average SOEE for an SFB operated from 1% SOC to 99% SOC is then given by

$$\mathrm{SOEE} = \frac{\sum_{i=m}^{n} \mathrm{SOEE_{ins}}(i\%\ \mathrm{SOC})}{n-m+1},\ (m=1, n=99)$$

Note that summation rather than integration is used here because the numerical calculation is already based on uniformly spaced discrete values of SOCs. For experimental data with non-uniformly spaced SOCs, integration should be used to calculate SOEE as the integral average of $\mathrm{SOEE_{ins}}$. By repeating the calculation described above with different $E_{cell}{}^0$ inputs, we can obtain the SOEE–$E_{cell}{}^0$ relationship in the $E_{cell}{}^0$ range of interest.

The modelling method presented above only considers the specific SFB devices studied in this work. Because the SFB was operated under a relatively low charging/discharging current density, the modelling method was simplified with some assumptions that may not hold true under higher current densities. Additional considerations and a revised method for modelling SFBs under more general operating conditions are presented in Supplementary Note 2. The method used in this study only considers the cell voltage profile of the SFB, so the I–V curve of the perovskite/silicon photoelectrode needs to be experimentally measured and used as input information before conducting the calculation. This method can be further revised with additional modelling for the photoelectrodes (such as using a diode equation) so that it can be generally used to estimate the SOEE–$E_{cell}{}^0$ relationship for other solar cells.

Integrated SFB device characterization. The integrated SFB device was assembled using a photoelectrode assembly and with all the other components the same as for the RFB device described in the previous section (Supplementary Fig. 17). The electrolyte flow rate was controlled at 20 ml min^{-1} for all the SFB cycling tests, if not specified otherwise. The SFB was kept in a nitrogen purge box (Terra Universal) during the SFB test.

To characterize the charging–discharging behaviours of the integrated SFB device, a Bio-Logic BP-300 bipotentiostat was used: channel 1 was configured as solar recharge mode to monitor the photocurrent; channel 2 was configured as RFB mode to monitor the potential difference between the two carbon felt electrodes (the connections for different modes are illustrated in Supplementary Fig. 18). During the solar recharging process, the perovskite/silicon photocathode was illuminated at near 100 mW cm^{-2} irradiance without applying any external bias until the cell potential measured by channel 2 reaching the upper cutoff potential of 1.5 V. During the discharging process, the illumination was blocked by an analogue signal regulated beam shutter, and the integrated device was operated as a normal RFB with a discharging current of −15 mA applied by channel 2 until the cell potential reached 0.8 V. The discharging current was selected to match the average solar recharging current. The light intensity was monitored using a solid-state silicon solar cell illuminated by the other branch of the light guide to ensure no substantial light intensity change during the SFB cycling test. Due to the natural irradiance decay of the Xe lamp in continuous operation, the power provided to the Xe lamp was manually adjusted during the cycling test to maintain a constant irradiance near 100 mW cm^{-2} (Supplementary Fig. 19a). The recorded illumination intensity was also used in the calculation of $\mathrm{SOEE_{ins}}$ and SOEE. The total capacity of the SFB device was measured by the galvanostatic–potentiostatic method before and after the SFB cycling test for several cycles with cutoff voltages of 0.8 V and 1.6 V, galvanostatic current density of 50 mA cm^{-2} and cutoff current density of 1 mA cm^{-2}.

The experimental $\mathrm{SOEE_{ins}}$ data as shown in Fig. 4b were calculated using the following equation:

$$\mathrm{SOEE_{ins}} = \frac{P_{electrical,out}}{P_{illumination}} \approx \frac{P_{electrical,in}\ \mathrm{PE_{internal}}}{P_{illumination}} = \frac{I_{operating} V_{operating}}{SA}\ \mathrm{CE}\times\mathrm{VE}$$

where $I_{operating}$ and $V_{operating}$ are extracted from data in the solar recharging half cycle (E_{cell} from 0.8 V to 1.5 V) as shown in Fig. 4a. S is 100 mW cm^{-2} and A is 1.0 cm^2. CE and VE are calculated using the following equations, respectively.

$$\mathrm{CE} = \frac{Q_{discharge}}{Q_{charge}} = \frac{\int I_{out}\, dt}{\int I_{operating}\, dt},\ \mathrm{VE} = \frac{\bar{V}_{discharge}}{\bar{V}_{charge}} = \frac{\frac{\int V_{out}\, dt}{\int dt}}{\frac{\int V_{operating}\, dt}{\int dt}}$$

where V_{out} is extracted from data in the discharging half cycle (E_{cell} from 1.5 V to 0.8 V) as shown in Fig. 4a. I_{out} is 15 mA. The experimental SOEE data as shown in Fig. 4c were calculated using the following equation:

$$\mathrm{SOEE} = \frac{E_{electrical,out}}{E_{illumination}} = \frac{\int I_{out} V_{out}\, dt}{\int SA\, dt}$$

Reporting Summary. Further information on research design is available in the Nature Research Reporting Summary linked to this article.

Data availability

Source data are provided with this paper. The remaining data that support the findings of this study are available from the corresponding author upon reasonable request.

Acknowledgements

This research is supported by the King Abdullah University of Science and Technology (KAUST) Office of Sponsored Research (OSR) under award no. OSR-2017-CRG6-3453.02 to both J.-H.H. and S.J. The Australian Centre for Advanced Photovoltaics (ACAP) encompasses the Australian-based activities of the Australia–US Institute for Advanced Photovoltaics (AUSIAPV) and is supported by the Australian Renewable Energy Agency (ARENA). J.Z. and A.H.-B. thank ARENA for support via project 2014 RND075. T.L.L., B.H. and M.H. acknowledge the US National Science Foundation (CAREER Award, grant no. 1847674) and Utah State University faculty start-up fund for support. B.H. and M.H. are grateful for China Scholarship Council (CSC) Abroad Studying Fellowships to support their PhD study at Utah State University. We thank Z. Wu for help with FcNCl synthesis, and D. Roberts and X. Liu for help with NMR.

Author contributions

W.L. and S.J. designed the experiments. W.L. fabricated the SFB devices and carried out the electrochemical measurements with the help of H.-C.F. and A.V. W.L. and Y.Z. built the customized control device for SFB characterization. J.Z. and A.H.-B. fabricated the perovskite/silicon tandem solar cells. B.H., M.H. and T.L.L. synthesized the N^{Me}-TEMPO and BTMAP-Vi redox couples. W.L. and S.J. wrote the manuscript and all authors commented on the manuscript.

Competing interests

The authors declare no competing interests.

Additional information

Supplementary information is available for this paper at https://doi.org/10.1038/s41563-020-0720-x.

Correspondence and requests for materials should be addressed to A.H.-B. or S.J.

nature research

Corresponding author(s): Song Jin, Anita Ho-Baillie

Solar Cells Reporting Summary

Nature Research wishes to improve the reproducibility of the work that we publish. This form is intended for publication with all accepted papers reporting the characterization of photovoltaic devices and provides structure for consistency and transparency in reporting. Some list items might not apply to an individual manuscript, but all fields must be completed for clarity.

For further information on Nature Research policies, including our data availability policy, see Authors & Referees.

Experimental design

Please check: are the following details reported in the manuscript?

1. Dimensions

Area of the tested solar cells	☒ Yes	Methods-Fabrication of photoelectrode assembly for the integrated SFB device
	☐ No	Explain why this information is not reported/not relevant.
Method used to determine the device area	☒ Yes	Methods-Fabrication of photoelectrode assembly for the integrated SFB device
	☐ No	Explain why this information is not reported/not relevant.

2. Current-voltage characterization

Current density-voltage (J-V) plots in both forward and backward direction	☒ Yes	Supplementary Fig. 22a.
	☐ No	Explain why this information is not reported/not relevant.
Voltage scan conditions *For instance: scan direction, speed, dwell times*	☒ Yes	Methods-Solid state and SFB solar cell characterization of perovskite/silicon cell
	☐ No	Explain why this information is not reported/not relevant.
Test environment *For instance: characterization temperature, in air or in glove box*	☒ Yes	Methods-Solid state and SFB solar cell characterization of perovskite/silicon cell
	☐ No	Explain why this information is not reported/not relevant.
Protocol for preconditioning of the device before its characterization	☐ Yes	State where this information can be found in the text.
	☒ No	No special preconditioning is needed before the device characterization
Stability of the J-V characteristic *Verified with time evolution of the maximum power point or with the photocurrent at maximum power point; see ref. 7 for details.*	☐ Yes	State where this information can be found in the text.
	☒ No	Since this work is more focused on the solar flow battery, the steady-state solar characteristics with time evolution was determined for the integrated solar flow battery, but not for the solar cell itself.

3. Hysteresis or any other unusual behaviour

Description of the unusual behaviour observed during the characterization	☐ Yes	State where this information can be found in the text.
	☒ No	No unusual behavior was observed during characterization
Related experimental data	☐ Yes	State where this information can be found in the text.
	☒ No	No unusual behavior was observed during characterization

4. Efficiency

External quantum efficiency (EQE) or incident photons to current efficiency (IPCE)	☐ Yes	State where this information can be found in the text.
	☒ No	This information can be found from a previous report using the same solar cell structure (ref.31 in manuscript). Since this work is focused on the integrated solar flow battery, these efficiencies are not in the scope of this work.
A comparison between the integrated response under the standard reference spectrum and the response measure under the simulator	☐ Yes	State where this information can be found in the text.
	☒ No	This is beyond the scope of this work. AM 1.5G solar simulator was used for all the characterizations.
For tandem solar cells, the bias illumination and bias voltage used for each subcell	☐ Yes	State where this information can be found in the text.
	☒ No	Not applicable for the characterization in this work.

5. Calibration

Light source and reference cell or sensor used for the characterization

- [x] Yes — *Methods-Solid state and SFB solar cell characterization of perovskite/silicon cell*
- [ ] No — *Explain why this information is not reported/not relevant.*

Confirmation that the reference cell was calibrated and certified

- [ ] Yes — *State where this information can be found in the text.*
- [x] No — *The silicon reference cell with the exact 1 cm2 area that matches with the solar cell samples was calibrated in-house with a certified reference cell.*

Calculation of spectral mismatch between the reference cell and the devices under test

- [ ] Yes — *State where this information can be found in the text.*
- [x] No — This is beyond the scope of this work. AM 1.5G solar simulator was used for all the characterizations.

6. Mask/aperture

Size of the mask/aperture used during testing

- [x] Yes — *Size of aperture is 1.0 cm2 for the data in Supplementary Fig. 4. No shadow mask was used for all the other measurements because no difference was found between the data collected with and without mask.*
- [ ] No — *Explain why this information is not reported/not relevant.*

Variation of the measured short-circuit current density with the mask/aperture area

- [ ] Yes — *State where this information can be found in the text.*
- [x] No — *The design area of the perovskite/silicon tandem in this work is 1.0 cm2.*

7. Performance certification

Identity of the independent certification laboratory that confirmed the photovoltaic performance

- [ ] Yes — *State where this information can be found in the text.*
- [x] No — This is not a photovoltaic cell per se and the reported efficiency is not the typical photovoltaic power conversion efficiency. No independent certification laboratory exists yet for certifying the performance of solar flow batteries.

A copy of any certificate(s)
Provide in Supplementary Information

- [ ] Yes — *State where this information can be found in the text.*
- [x] No — see above

8. Statistics

Number of solar cells tested

- [ ] Yes — *State where this information can be found in the text.*
- [x] No — The final integrated solar flow battery device is not a solar cell per se. The focus of this work is the match between solar cell and redox couples, which doesn't rely on the number of solar cells tested.

Statistical analysis of the device performance

- [ ] Yes — *State where this information can be found in the text.*
- [x] No — see above

9. Long-term stability analysis

Type of analysis, bias conditions and environmental conditions
For instance: illumination type, temperature, atmosphere humidity, encapsulation method, preconditioning temperature

- [x] Yes — *Methods-Integrated SFB device characterization*
- [ ] No — *Explain why this information is not reported/not relevant.*